Revealing the Mechanism of Protein-Lipid Interactions for a Putative Membrane Curvature Sensor in Plant Endoplasmic Reticulum

Rhiannon L. Brooks [1, 2] and Ann M. Dixon [2] *

[1]MAS Centre for Doctoral Training, University of Warwick, Coventry, CV4 7AL, UK;

[2]Department of Chemistry, University of Warwick, Coventry, CV4 7AL, UK;

*Correspondence: ann.dixon@warwick.ac.uk

ABSTRACT

Membrane curvature sensing via helical protein domains, such as those identified in Amphiphysin and ArfGAP1, have been linked to a diverse range of cellular processes. However, these regions can vary significantly between different protein families and thus remain challenging to identify from sequence alone. Greater insight into the protein-lipid interactions that drive this behavior could lead to production of therapeutics that specifically target highly curved membranes. Here we demonstrate the curvature-dependence of membrane binding for an amphipathic helix (APH) in a plant reticulon, namely RTNLB13 from A. thaliana. We utilize solution-state nuclear magnetic resonance spectroscopy to establish the exact location of the APH and map the residues involved in protein-membrane interactions at atomic resolution. We find that the hydrophobic residues making up the membrane binding site are conserved throughout all A. thaliana reticulons. Our results also provide mechanistic insight that leads us to propose that membrane binding by this APH may act as a feedback element, only forming when ER tubules reach a critical size and adding stabilization to these structures without disrupting the bilayer. A shallow hydrophobic binding interface appears to be a feature shared more broadly across helical curvature sensors and would automatically restrict the penetration depth of these structures into the membrane. We also suggest this APH is highly tuned to the composition of the membrane in which it resides, and that this property may be universal in curvature sensors thus rationalizing the variety of mechanisms reported for these functional elements.

Keywords: Plant reticulon, membrane curvature sensor, amphipathic helix, model membranes, nuclear magnetic resonance

INTRODUCTION

The sensing and modulation of membrane curvature by surface associated α-helices has emerged as an important mechanism for protein function and membrane remodeling, with increasing numbers of these regions being reported over the past decade (Drin and Antonny, 2010). The idea that membrane morphology is a viable recognition element capable of high affinity interactions with proteins has far reaching implications given that critical cellular processes often localize to curved membranes. Examples of this are summarized in more detail in a recent review (Jarsch *et al.*, 2016), and include receptor mediated endocytosis (Ford *et al.*, 2002), assembly of the nuclear pore complex (Vollmer *et al.*, 2012), cell maturation (Ramamurthi *et al.*, 2009), cell division (Ramamurthi and Losick, 2009), immune function (He and Bongrand, 2012) and viral infection (Maier *et al.*, 2010). A better understanding of protein-membrane interactions in regions of high curvature could direct engineering of therapeutics that target these regions and the functions that occur therein. Indeed, this has been demonstrated for a curvature sensing peptide called MARCKS-ED, which has been used to target highly-curved, PS–rich extracellular vesicles (Morton *et al.*, 2013).

However, curvature-sensing regions are currently difficult to identify from sequence alone, and often require a large degree of prior knowledge for the proteins in which they reside (Antonny, 2011; Giménez-Andrés *et al.*, 2018). There is also a clear lack of high-resolution structural information defining the molecular requirements for binding in these regions. The situation is further complicated by the fact that no universal mechanism of membrane association can be applied to currently known curvature sensing regions. Some curvature sensors, such as those in complexin (Snead *et al.*, 2014) and the Golgi-localized ArfGAP1 (Bigay *et al.*, 2005; Vanni *et al.*, 2014), are thought to associate with curved membrane surfaces via interaction of the hydrophobic face of an amphipathic helix (APH) with the exposed lipid hydrocarbon chains of the membrane interior, henceforth described as lipid-packing defects, found on highly curved membranes (Figures 1A-B). Other curvature sensors, such as α-Synuclein (Figure 1C) and the putative APH

in Yop1p (Brady *et al.*, 2015), associate with curved membranes via a combination of electrostatic interactions with anionic lipid head groups and interaction with lipid-packing defects (Jao *et al.*, 2008; Jensen *et al.*, 2011; Pranke *et al.*, 2011). Still other curvature sensors interact with curved membranes via oligomerization of banana-shaped helical domains, as is the case with the BAR domain (Casal *et al.*, 2006). This lack of consensus, coupled with a paucity of structural data, holds back understanding of this unique source of selectivity and the ability to exploit it.

Recently discovered APHs in two different reticulon proteins (RTNs), namely the yeast RTN Yop1p (Brady *et al.*, 2015) from *Saccharomyces cerevisiae* and the plant reticulon RTNLB13 (Breeze *et al.*, 2016; Chow *et al.*, 2018) from *Arabidopsis thaliana* are also speculated to comprise curvature sensing and/or modulating elements. The presence of a curvature-sensitive region in RTNs is fitting as these proteins play a key role in generation of highly-curved tubules during endoplasmic reticulum (ER) membrane remodeling in eukaryotes (Hu *et al.*, 2008; Voeltz *et al.*, 2006). RTNs are thought to drive formation of ER tubules through a “wedging and scaffolding” mechanism involving a region known as the reticulon homology domain (RHD, see Figure 2) (Oertle *et al.*, 2003; Schweitzer *et al.*, 2015; Shibata *et al.*, 2008; Sparkes *et al.*, 2010) present in all RTNs. The APH, proposed to be conserved throughout the DP1 family as well as *all* RTN family proteins, is located near the C-terminus of the RHD. Removal of this region from the full-length protein lead to reduction or elimination of membrane shaping activity (*in vitro* and *in vivo*), suggesting that the APH is a key structural requirement in this class of protein. In the case of RTNLB13, which consists of a single RHD and as such is a model for the minimal functional RTN, we predicted the location of a 16-residue APH (Breeze *et al*., 2016) and showed that a peptide derived from this region could form an α-helix in detergent micelles. We have also demonstrated the existence of additional helical regions outside of the transmembrane (TM) domains in full-length RTNLB13 (Chow *et al.*, 2018). However, beyond identifying its presence, very little is known about the structure of this APH, its mode of interaction with the membrane bilayer, and most importantly its role in membrane-shaping. Given the biological importance of ER remodeling,

with deformities in ER morphology leading to diseases such as Alzheimer's disease and hereditary spastic paraplegia (Westrate *et al.*, 2015), an atomic description of the interaction between the APH and model membranes is of great interest.

Here, we demonstrate experimentally the curvature-dependence of membrane-binding for the APH in RTNLB13 from *A. thaliana*. Such a property has not been demonstrated for similar regions in any reticulon protein thus far. We identified those residues within the APH that are directly interacting with the membrane, and find that the hydrophobic residues that comprise this binding interface are conserved throughout all *A. thaliana* reticulons. We hypothesized that this shallow hydrophobic face restricts how far the APH can penetrate into the membrane and that this APH appears to be highly tuned to the lipid composition of the membrane with which it associates. Furthermore, we hypothesize that these features are broadly characteristic of helical curvature sensors, thus accounting for the range of mechanisms that have been reported thus far in the literature.

RESULTS

Residues E_{160}-K_{175} in RTNLB13 contain an amphipathic helix that is curvature-responsive and displays some requirement for ionic lipids

As mentioned above, we have recently demonstrated that removal of residues Glu_{160}–Lys_{175} from RTNLB13 inhibits tubule formation in the ER membranes of *A. thaliana* (Breeze *et al*., 2016). To investigate the physical properties that induce helix formation in this region of RTNLB13, a 16-residue peptide (R13-APH_{16} in Figure 2C) composed of residues Glu_{160}–Lys_{175} was synthesized, purified, and reconstituted into a wide range of membrane mimetics (Table 1). Our library of fourteen different membrane mimetics included three detergents varying in surface charge and aggregation number, synthetic membrane bilayers of varying lipid composition, acyl chain lengths, saturation, and head group charge, and lipid bicelles composed of short- and long-chain lipids. Peptide folding was studied across the library of membrane mimetics using circular dichroism

(CD) spectroscopy, and the data were fit using Dichroweb software (Whitmore and Wallace, 2004) to obtain an estimate of secondary structure content. As shown in Figure 3A, CD data indicated that this peptide is soluble but has no defined structure (random coil) in aqueous buffer solution. Upon addition of micelles composed of anionic detergent (1-myristoyl-2-hydroxy-sn-glycero-3-phospho-(1'-rac-glycerol), LMPG) or zwitterionic detergent (DPC), an α-helical content of 55% or 37%, respectively, was estimated for R13-APH$_{16}$. Addition of increasing concentrations of these two detergent micelles lead to a dose-dependent increase in negative ellipticity at 222 nm (shown for LMPG in inset, Figure 3A), indicating that micelle binding induces helix formation. The helical content of R13-APH$_{16}$ was lost (3–10% helicity, which we interpret as negligible for a peptide of this length) and the peptide remained unstructured when combined with nonionic detergent n-dodecyl-β- D-maltoside (DDM, Figure 3A) or any of the lipid vesicles in our library (see Table 1 for all values and Figure 3B for a representative CD spectrum in 1,2-dimyristoyl-sn-glycero-3-phosphocholine, DMPC). This was observed regardless of whether a net negative charge was present on the vesicle surface.

Only when short-chain lipids were mixed with long-chain lipids, to create lipid bicelles with *q* values (*q* = [DMPC]/[DHPC]) ranging from 0.25–0.75, was the helicity of the peptide detectable once again (Figure 3B). This behavior suggested a link between the curvature of the membrane mimetic and folding of R13-APH$_{16}$. Dynamic light scattering was used to measure the hydrodynamic diameters of all membrane mimetics tested, and the resulting diameters are given in Table 1. Our mimetics provided good coverage of diameters between 3-83 nm, and a plot of helical content of the R13-APH$_{16}$ peptide versus diameter of the mimetic is shown in Figure 3C. This plot shows a clear relationship between diameter and helical content of the putative RTNLB13 APH, and indicates that this region is only able to fold in the presence of membrane mimetics with diameters ≤ 18 nm. To validiate that these results were reporting curvature, and not some other aspect of our chemically-diverse library, two well-known curvature sensors (residues 2-23 of human α-synuclein and the ALPS motif in rat ArfGAP1, residues 199-223) were also

exposed to the entire library of mimetics. As shown in the inset to Figure 3C, these two positive controls closely mirror the results obtained for the R13-APH_{16} peptide.

Solution state NMR was used to determine the location of the helix within the R13-APH_{16} peptide sequence. ^{1}H-^{1}H TOCSY and ^{1}H-^{1}H NOESY spectra were used to sequentially assign the peptide (Table S1 and Figure S1) and reveal long-range NOEs in the presence of DPC micelles, which yielded significant helical structure and were available in a fully deuterated form. 63% of the ^{1}Hs in the R13-APH_{16} peptide were assigned in DPC, and these assignments were used to construct an NOE-derived map of backbone NH, Hα and Hβ connectivities and perform a $^{1}Hα$ chemical shift index (CSI) analysis (Wishart *et al.*, 1992) as shown in Figure 4. The NMR data were indicative of α-helix formation between residues Glu_{160}–Leu_{169}, which agrees well with results from CD. Together these data demonstrate that this region of a plant reticulon contains a curvature-responsive helix that requires *both* surface charge and high curvature to fold, similar to α-synuclein (Jensen *et al.*, 2011). The results also map the helix to the extreme N-terminus of the peptide.

Amphipathic helix extends beyond predicted region, and inclusion of entire helical region alters the determinants of membrane interaction

The well-known difficulties in predicting curvature-responsive regions from sequence alone coupled with the location of the APH at the extreme N-terminus of the R13-APH_{16} peptide lead us to ask if the helix extended beyond this region. Our previous analyses of the putative location of the TM domains suggested that the fourth TM domain may end as early as residue Val_{154} (Chow *et al.*, 2018). Therefore, we created two additional peptides to more thoroughly explore sequence space in this region of RTNLB13. An 18-residue peptide, spanning Val_{154}–Ser_{171} (R13-$APH_{18,}$ Figure 2C), was used to extend the N-terminus of the peptide by six residues without dramatically changing the length of the peptide. A 22-residue peptide (Val_{154}–$Lys_{175,}$ R13-APH_{22}) spanned the entire sequence covered by *both* other peptides and was studied to ensure that the entire

continuous helix was captured. Both peptides fit the general trend expected for an APH, containing a polar/charged face and a hydrophobic face when plotted around a helical wheel (Figure 5A) and yielding higher hydrophobic moments (μ_{18} = 8.58, μ_{22} = 9.99) than the original R13-APH$_{16}$ peptide (μ = 6.85). This region of RTNLB13 is also well-conserved across 19 of the 21 RTNLB isoforms found in *A. thaliana* (Figure S2).

These longer peptides showed significant helical content in all three detergent types, as summarized in Table 1 and Figures S3–4, and no longer exhibited a requirement for anionic head groups in order to fold. Indeed, the requirement for negative charge seems to be completely lost in the 22-residue peptide, which folds equally well in all micelle types. Increasing detergent concentrations lead to a dose-dependent increase in negative ellipticity at 222 nm (inset, Figures S3A and S4A) indicating that micelle binding induced helix formation in all detergents tested. Peptide folding was also studied in lipid vesicles and bicelles as before, and both peptides retained the sensitivity to curvature that was demonstrated for the R13-APH$_{16}$ sequence. Figure 5B shows the reduction in helical content for R13-APH$_{18}$ and R13-APH$_{22}$ as the average diameter of the membrane mimetic was increased. In both cases, the peptides are only able to fold at diameters ≤ 27 nm.

Solution-state NMR was again used to map the location of the helix within each DPC-solubilized peptide as before (see Tables S2–S3 for assignment and Figure S5 for representative data). The NOE-derived map of backbone NH, Hα and Hβ connectivities and ^{1}Hα CSI analysis for the R13-APH$_{22}$ peptide (Figure 5C) localized the helix between residues Lys$_{156}$–Leu$_{169}$. The same 14-residue region was identified from the analogous data for the R13-APH$_{18}$ peptide, and these results are summarized in Figure S6. The length of the APH described in each peptide correlated to a helical content of 78% and 64% in R13-APH$_{18}$ and R13-APH$_{22,}$ respectively and these values were in excellent agreement with the results from CD (79% and 69% respectively).

Residues Lys_{156}–Leu_{169} also encompass the most highly conserved positions in this region, as shown in the sequence logo in Figure 5D.

Curvature responsive region does not stably bind to membranes in a disordered conformation

The CD data used above to probe binding to membrane bilayers required the generation of long-lived secondary structure to report peptide-membrane interactions. However, it has been reported that a curvature-sensing amphipathic region at the C-terminus of complexin, responsible for inhibition and localization of the protein to synaptic vesicles, can bind to membranes in either a helical or disordered conformation (Snead *et al.*, 2014). Fluorescence spectroscopy and diffusion-ordered NMR spectroscopy (DOSY) are methods that do not require helix formation to report binding, and were thus selected to probe the binding of unfolded peptide to membrane mimetics. Both the R13-APH_{18} and R13-APH_{22} peptides contain a native Trp residue (Trp_{158}) which was monitored to gauge the polarity of the peptide environment. The fluorescence emission wavelength (λ_{em}) of the Trp residue undergoes a substantial blue shift (to lower wavelength) upon moving from an aqueous environment to the apolar environment of the membrane mimetic. Fluorescence data are shown in Figure 5B (inset) for the R13-APH_{18} peptide solubilized in aqueous buffer, DPC detergent, and DMPC vesicles. These mimetics were selected because they represent conditions in which high as well as minimal helical content was observed by CD. The analogous data for the R13-APH_{22} peptide are given in Figure S7A. In both cases, the identical trend was observed in which Trp emission was observed at λ_{em} = 360 nm in aqueous buffer, and experienced a 20 nm blue shift to λ_{em} = 340 nm when DPC was present, suggesting partitioning of Trp to a non-polar environment. However, no blue shift was observed when DMPC was present, suggesting that neither peptide participates in a long-lived binding interaction with the vesicles.

These results were supported by DOSY NMR measurements made for the R13-APH$_{22}$ peptide in the absence and presence of DPC micelles and DMPC vesicles. Table 2 summarizes the diffusion coefficients obtained from peptide solubilized in aqueous buffer, 50 mM DPC, or 2.4 mg/mL DMPC, and a typical fit of the data is shown in Figure S7B. These values were used, along with the diffusion coefficients measured for "free" DPC micelles and DMPC vesicles, to estimate the fraction of peptide bound as described in the Materials and Methods, and indicate complete (i.e. 100%) binding of the peptide to DPC and negligible (~2%) binding to DMPC vesicles. The results above show that (on the timescale of these measurements) there is no detectable population of unfolded vesicle-bound peptide, as was observed for complexin, and support a model in which this interaction is either absent or very short-lived.

Curvature-responsive region folds in small, highly stable unilamellar phospholipid vesicles

To test our conclusion that this APH has an affinity for high curvature, and not an affinity for detergent molecules (in which the highest helicity was observed), we wished to create a small unilamellar vesicle with a diameter near 27 nm to reflect the results from CD and DLS above. Several attempts were made to create "tiny" vesicles by extended sonication and/or freeze-thaw cycles, extrusion through membranes with decreasing pore sizes down to 15 nm, and incorporation of conical lipids (e.g. PE) into the preparation (data not shown). None of these approaches yielded stable vesicles with diameters below 36 nm, and these vesicles were highly unstable over time. A review of the literature revealed that creation of stable lipid vesicles with diameters < 30 nm has not been well-demonstrated. Very few reports exist in which sufficient data is provided to support successful preparation of small and stable vesicles, with the smallest vesicle diameters ranging from 35-46 nm (Pitcher III and Huestis, 2002; Yue *et al.*, 2005). Using a method published by Yue et al. (Yue *et al.*, 2005), in which small unilamellar vesicles with a composition of 60:1:15 DMPC:DMPG:DHPC form via spontaneous vesiculation, we obtained

stable vesicles with an average diameter of 23 nm (see Figure S8A). Addition of these vesicles to the R13-APH_{22} peptide yielded a clear helical signal in the CD spectrum (Figure 6) that corresponded to 25% helical content. Using the identical membrane composition above, we then prepared vesicles of increasing diameter up to 116 nm and recorded CD spectra of the peptide. The resulting spectra are shown in Figure 6 along with a plot of mean residue ellipticity at 222 nm and percentage helical content vs. vesicle diameter (inset). These data are well-described by the trend shown in Figure 5B and support the conclusion that what we observe in detergents is a report of curvature sensing and not an artifact. This may be a reflection of the widely-accepted theory that curvature sensing helices likely interact with membrane packing defects in curved membranes. It has been demonstrated in previous studies that detergent molecules within a micelle (D. P. Tieleman *et al.*, 2000; Dixon *et al.*, 2002) and lipid molecules within bicelles of $q < 1$ (Caldwell *et al.*, 2018) are loosely packed and dynamic, and thus may resemble these defects and provide an excellent platform upon which to investigate curvature-sensing helices at atomic resolution. Of course, any results obtained in this way must be corroborated *in vivo* to demonstrate the biological role, as we have done for RTNLB13 in our previous work (Breeze *et al.*, 2016).

Curvature-responsive folding occurs via a shallow hydrophobic face defined by highly conserved aromatic and hydrophobic residues

Apart from a single Ile residue (I_{165}), which when mutated to Lys yielded a reduction in tubule formation in RTNLB13 *in vivo* (Breeze *et al.*, 2016), the molecular determinants for APH-membrane interactions remain unknown. To identify residues within the APH that are directly interacting with highly curved membranes, deuterium exchange and saturation transfer difference NMR (STD-NMR) were applied. The amide and aromatic region of the ^1H spectrum of the R13-APH_{22} peptide in DPC micelles is shown in Figure 7A for comparison with the deuterium exchange spectrum in Figure 7B, in which labile protons could exchange with deuterium upon dissolution of the peptide in D_2O. The exchange spectrum was acquired 10 minutes after the addition of D_2O to

a lyophilized sample containing peptide and fully protonated DPC detergent. Signals from non-labile aromatic ^{1}Hs remained in the spectrum, while the majority of the backbone H_N peaks in the spectrum were fully attenuated before data were acquired. However, exchangeable NH ^{1}Hs from Gln_{166}, Tyr_{161}, Gly_{162}, and Ile_{165} remained in the spectrum and were protected from exchange relative to the rest of the sequence, suggesting that these residues were interacting directly with the micelle.

An alternative method, namely STD-NMR, was used to validate these results. In STD-NMR, selective saturation of a host can be transferred to protons in a ligand via the nuclear Overhauser effect if those protons are within 5 Å of the host (Mayer and Meyer, 1999). This yields NOE enhancement of the signals from "bound" protons within the ligand after subtraction of the on-resonance ^{1}H spectrum (acquired upon selective irradiation of the host) from the off-resonance spectrum (acquired with no saturation of the host). Signals that remain in this difference spectrum identify which protons in the ligand form the binding epitope with the host.

In this work, the membrane mimetic was defined as the "host" and RTN-APH_{22} peptide as the "ligand", and to our knowledge this is one of very few demonstrations of this approach. Spectra were acquired for samples containing the RTN-APH_{22} peptide in 100% D_2O buffer and fully protonated DPC micelles, in which a suitable on-resonance frequency was identified at -2.0 ppm in which no saturation of peptide was detected. Difference spectra were collected using saturation times (t_{sat}) ranging from 0.25–5.0 seconds in order to follow the buildup for all ^{1}Hs displaying saturation transfer. A plot of STD amplification factor (STD-AF) versus saturation time is given in Figure S8, and the difference spectrum collected with a t_{sat} = 1 second is shown in Figure 7C. While the requirement to carry out STD-NMR experiments in 100% D_2O buffer meant that all labile protons (*i.e.* backbone NH) were fully exchanged at the time of acquisition, the spectra clearly reveal efficient saturation transfer from the DPC micelle to a subset of ^{1}Hs in the RTN-APH_{22} peptide. The signals in the STD spectra implicated protons in the aromatic rings of Trp_{158}, Tyr_{161}, and His_{168} in the binding of the peptide to the micelle.

The H-D exchange and STD NMR results are summarized in Figure 7D on a helical wheel containing the 14-residue sequence we have identified as containing the curvature-responsive helix in RTNLB13. Residues protected from H-D exchange and sensitive to saturation transfer all map to a discrete face of the helix that is shared by Ile_{165}, the only residue known to significantly impact ER tubule formation *in vivo* when mutated in this family of reticulons. The hydrophobic face of the APH shown in Figure 7D could partition into the hydrophobic core via two aromatic residues that are completely conserved across all reticulon isoforms in *A. thaliana* (see positons 5 and 8 in Figure 5D), suggesting their importance in function. The polar Gln and His residues that flank this hydrophobic face could interact with lipid head groups, and the highly conserved charged face of this helix would be oriented toward the aqueous environment.

DISCUSSION

Here we demonstrate the curvature-dependence of membrane binding and folding for a region in a plant reticulon, RTNLB13 from *A. thaliana*, previously demonstrated to be critical for ER membrane remodeling from tubules to sheets *in vivo* (Brady *et al.*, 2015; Breeze *et al.*, 2016) and speculated to be present in nearly all members of the reticulon family (Brady *et al.*, 2015; Breeze *et al.*, 2016). Despite these facts, such a property has not been demonstrated for similar regions in any reticulon family member until now. Our work indicates the presence of a membrane curvature sensor in the C-terminus of the protein. The helical features of this region emerged only when the hydrodynamic diameter of the membrane mimetic was between 3–27 nm, with helicity increasing as diameter decreased. This result is noteworthy when compared to the reported diameters of various plant tubules formed *in vivo* (20–50 nm) (Miyashita and Koga, 2017) and *in vitro* (30 nm) (Yokota *et al.*, 2011), yeast tubules formed *in vivo* (30 nm) (West *et al.*, 2011), and tubules formed *in vitro* by reticulon-like proteins (*e.g.* 17 nm for Yop1p (Brady *et al.*, 2015) and 25 nm for poxvirus A17 (West *et al.*, 2011)). The tubule diameters in these studies compare favorably with the emergence of observable helicity in our data, especially if one considers that the portion

of a spherical micelle / vesicle to which the rod-like APH will bind can be approximated by a cylindrical “slice” of that sphere, the curvature of which would be very similar to that in a cylinder of equal diameter. While it cannot be ruled out that the lack of binding to larger vesicles we observe here may be exacerbated by the removal of the APH from the full-length protein, the curvature-sensitivity may suggest that this APH is highly adapted to form only in the presence of membrane surfaces with a specific size and number of membrane packing defects, a typical consequence of high curvature. Such specificity is an exciting prospect as it implies this feature of membranes could be targeted in future applications.

As mentioned earlier, curvature-sensing regions are not defined by a single membrane-binding mechanism and are notoriously difficult to accurately locate from sequence alone, and the homologous region in the RTNLB13 protein is no different. We have located the 14-residue curvature sensing helix using solution state NMR, and found that our original estimate of the location of this helix (R13-APH$_{16}$, (Breeze *et al.*, 2016)) omitted four residues including a completely conserved hydrophobic aromatic residue that we now know forms part of the membrane interaction site (W$_{158}$). Most importantly, this subtle change in sequence significantly altered the determinants of membrane binding, removing any dependence upon electrostatic interaction with anionic lipids. We propose that this is by design, as dependence on specific charged lipids would be a liability in the ER. Not only is plant ER composed predominantly of uncharged lipids, with compositions of 51% PC/33% PE being reported (Coughlan *et al.*, 1996), but the ER membrane is a highly dynamic environment and the site of lipid synthesis and transport (Griffing *et al.*, 2017). The curvature sensor identified in this work is not reliant on charge to fold, and we suggest this adaptability would be highly advantageous in the ER membrane. More broadly, we suggest this curvature sensor is highly tuned to the lipid composition of the membrane in which it resides, and that this property may be universal in curvature sensors thus rationalizing the variety of mechanisms reported.

Our data also provide rare mechanistic insight into direct protein–membrane interaction sites within this curvature responsive region. Four hydrophobic residues make up a hydrophobic helical face that interacts with membrane mimetics (Figure 7D). One of these residues is I_{165} which, when mutated to Lys, resulted in a loss of tubule-forming ability in the full-length protein (Breeze *et al.*, 2016). The two aromatic residues in this interaction face are completely conserved throughout all 21 isoforms in *A. thaliana*, and indeed are the only completely conserved sites in the entire APH region. We propose that the shallow hydrophobic face we identify here is broadly characteristic of all curvature sensing helices, including the amphipathic lipid packing sensors (ALPS) in the ArfGAP1 protein and in α-synuclein (Figure 7E), restricting the depth to which these helices can penetrate into the hydrophobic core of the bilayer. This is in keeping with the role of these regions as sensors and stabilizers of highly curved membrane structures, and distinguishes them from other amphipathic helices such as those formed by antimicrobial peptides. Peptides such as Aurein, Magainin 1, and Mastoparan (Figure 7E) contain hydrophobic helical faces that encompass $\geq$ 50% of the sequence and are thus able to penetrate deeply into the membrane core. This feature affords the ability to efficiently destabilize cell membranes via a number of reported mechanisms (Sato and Feix, 2006). Such a large and destabilizing hydrophobic region would be ill-advised in a curvature sensor.

In the case of the plant reticulon under investigation here, our results lead us to propose a new model for function that now includes this curvature responsive region. Insertion of the RHD TM domains into the ER membrane generates local membrane curvature via wedging and scaffolding, as previously reported for reticulons (Shibata *et al.*, 2008). Formation of ever-larger RTN oligomer “networks” generates further membrane curvature and introduces lipid defects of increasing number and size. It is likely that once sufficient numbers of defects are present, the APH region will bind/insert into these via interactions between the hydrophobic face of the APH and exposed fatty acyl chains present in lipid packing defects. We suggest that membrane binding

by the APH may act as a feedback element, only forming when ER tubules reach a critical size and adding stabilization to these structures without disrupting the bilayer.

MATERIALS AND METHODS

Synthesis and purification of RTNLB13 APH, α-Synuclein and ArfGAP1 peptides

Three peptides corresponding to residues 160–175 (R13-APH$_{16}$), 154–171 (R13-APH$_{18}$), and 154–175 (R13-APH$_{22}$) of RTNLB13 from *A. thaliana,* with the sequences EYGDQIQKHLGSLKDK (M_W 1859.07), VPKLWEEYGDQIQKHLGS (M_W 2127.38), VPKLWEEYGDQIQKHLGSLKDK (M_W 2611.98) respectively, and two peptides corresponding to residues 2-23 of human α-Synuclein and residues 199-223 of ArfGAP1 from *R. norvegicus,* with the sequences DVFMKGLSKAKEGVVAAAEKTK (M_W 2307.73) and FLNSAMSSLYSGWSSFTTGA SKFAS (M_W 2634.90) respectively, were synthesized using F-moc chemistry and purified to 95% purity at Insight Biotechnology Limited (Wembley, UK). Peptide purity was confirmed by HPLC and electrospray ionization time-of-flight mass spectroscopy (ESI-TOF-MS microTOF, Bruker) before subsequent lyophilization. The peptides were stored as dry powders at -20°C until use.

Vesicle and bicelle preparation

Vesicles with a variety of lipid compositions (summarized in Table 1) were generated by dissolving lipid in a mixture of 3:1 chloroform:methanol to a final concentration of 10 mg/mL, and drying to a film on a rotary evaporator. The samples were then placed under vacuum to ensure complete removal of the organic phase. The resulting lipid film was reconstituted in 25 mM sodium phosphate buffer, pH 6.6, to a final concentration of 3.3 mg/mL and subjected to four freeze-thaw cycles, followed by sonication at 40 °C for 5 min. Vesicles were extruded through polycarbonate membranes (Avanti Polar Lipids) with pore diameters of 50 nm before use. Bicelles were prepared from 1,2-dimyristoyl-sn-glycero-3-phospho- choline (DMPC) and 1,2-dihexanoyl-sn-glycero-3-phosphocholine (DHPC) with *q* values ranging from 0.25–0.75 (*q* = [DMPC]/[DHPC]) and a total lipid concentration of 150 mM by mixing the appropriate amount of DMPC with 25 mM sodium

phosphate buffer, pH 6.6, vortexing and centrifuging the sample repeatedly until a homogeneous slurry was formed, and then adding an appropriate amount of a 400 mM DHPC stock solution. This mixture was then subjected to several cycles of centrifugation and vortexing until a clear non-viscous solution was obtained. All lipids were purchased from Avanti Polar Lipids (Alabaster, AL) and used without further purification.

Circular Dichroism

CD spectra were measured using a Jasco J-1500 spectropolarimeter equipped with a Peltier thermally controlled cuvette holder (Jasco UK, Great Dunmow, UK) and 1.0 and 0.1 mm path length quartz cuvettes (Starna, Optiglass Ltd, Hainault, UK). All spectra were recorded over the wavelength range 190–300 nm using a 2.0 nm spectral bandwidth, 0.2 nm step resolution, 200 nm/min scanning speed, and 1 s response time. All CD spectra shown were collected at 37 °C, and were averaged from sixteen individual spectra after subtraction of the CD spectrum of the buffer. The peptide samples were prepared in 25 mM sodium phosphate buffer, pH 6.6, in the presence and absence of a membrane mimetic at increasing concentrations, maintaining a constant peptide concentration typically in the range of 50–75 μM. Protein concentrations were determined using the absorbance of the protein at 280 nm (A_{280}) and Beers law. The machine units of millidegrees were converted to mean residue ellipticity to normalize to protein concentration. CD data was fit using DichroWeb (Chen et al., 2011) (Contin (van Stokkum et al., 1990)/training set 4 (Sreerama and Woody, 2000)) to estimate the secondary structure content.

Fluorescence Spectroscopy

Intrinsic fluorescence of the tryptophan residue in the R13-APH_{18} and R13-APH_{22} peptides was measured before and after the addition of different concentrations of either DMPC lipid vesicles or DPC micelles. A peptide concentration of 47 μM was used for R13-APH_{18}, whereas only 5 μM of R13-APH_{22} was used, in a 3.0 mm pathlength quartz cuvette. Fluorescence intensity was measured at 20 ^{o}C with a Jasco FP-6500 (Jasco UK, Great Dunmow, UK) spectrofluorometer, equipped with a Jasco

ADP-303T temperature controller. Excitation was set to 280 nm, whilst emission spectra were recorded from 300 to 450 nm at a bandwidth of 3 nm. Correction for light scattering was carried out by subtraction of the corresponding spectra of the membrane mimetics.

Dynamic Light Scattering

An estimate for the hydrodynamic diameter of each membrane mimetic, diluted to a concentration of 0.06 mg/ml with 25 mM sodium phosphate buffer at pH 6.6, was measured by dynamic light scattering using a Zetasizer Nano-series instrument (Malvern Instruments, UK) at room temperature, with UV-transparent disposable cuvettes of 1 cm path length. All spectra were collected after 300 s equilibration time and averaged from six individual spectra. Data was processed using the Malvern Zetasizer software and exported as intensity and number distributions.

Nuclear magnetic resonance experiments

RTNLB13 APH peptide samples for NMR analyses were prepared by dissolving the peptides to a final concentration of 1–1.5 mM in 25 mM sodium phosphate buffer, pH 6.6, 90% H_2O, 10% D_2O, containing 50 mM DPC-d_{38}. All spectra were collected at 37 °C on an Avance 700 MHz spectrometer (Bruker Biospin, UK) equipped with a triple resonance inverse cryoprobe with Z-gradients and referenced to residual water. ^{1}H-^{1}H TOCSY and NOESY spectra were collected with 4096 × 256 data points, 14 × 14 ppm spectral windows, 32 scans and mixing times ranging from 70–140 ms and 90–200 ms, respectively. Spectra were processed using Topspin 3.2 and assigned using CCPNmr Analysis (Vranken *et al.*, 2005). STD-NMR experiments were performed on samples of R13-APH_{22} in 100% D_2O buffer with 25 mM sodium phosphate, pD 7.0, prepared with and without 50 mM DPC, and a pseudo-2D version of the STD NMR sequence was used for the interleaved acquisition of off- and on-resonance spectra: 1D STD with spoil and T2 filter using excitation sculpting for water suppression (Mayer and Meyer, 1999). Off- and on-resonance spectra were acquired separately and subtracted manually to obtain the STD spectrum. For selective saturation, the on-resonance frequency was set to -4692 Hz (-2 ppm), whereas the off-

resonance frequency was set to 30000 Hz (42.8 ppm). Blank experiments (in the absence of DPC) were performed to test the lack of direct saturation to peptide protons and select the appropriate on-resonance frequency. Saturation time was varied from 0.25–5 s, and the relaxation delay was held at 5.5 s. The spectral window size was 14 × 2.85 ppm, the number of data points was 32768 × 4 and the number of scans was 8. Deuterium exchange experiments were performed on samples of R13-APH_{22} solubilized in 25 mM sodium phosphate, pD 7.0, containing 50 mM DPC and prepared in 100% D_2O. 1D ^1H spectra were acquired 10 minutes after the addition of D_2O to lyophilized peptide and detergent samples, with a spectral window size of 14 ppm and 16 scans. Peptide diffusion coefficients were calculated using ^1H data obtained from pseudo-2D diffusion ordered spectroscopy (DOSY) experiments (Wu *et al.*, 1995), with a spectral window size of 14 × 14 ppm, 16384 × 16 data points, 30–400 ms diffusion delay time, 5 ms eddy current delay time, and 128 scans. DOSY data was processed using the T1/T2 relaxation module within Topspin 3.2, and all diffusion coefficients are reported for samples prepared in 100% D_2O buffer.

Bioinformatics

Full-length sequences of RTNLB proteins were obtained from UniProt (UniProt: a worldwide hub of protein knowledge, 2019), and sequence alignment/formatting was carried out using Clustal Omega (Madeira *et al.*, 2019). The sequence logo was produced using Weblogo 3 (Crooks *et al.*, 2004). Helix representations were generated using Chimera (Pettersen *et al.*, 2004).

ACKNOWLEDGEMENTS

RLB thanks EPSRC for a PhD studentship through the EPSRC Centre for Doctoral Training in Molecular Analytical Science, grant number EP/L015307/1. The authors wish to thank I. Prokes (University of Warwick, Coventry, UK) for NMR assistance and Prof. L. Frigerio (University of Warwick, Coventry, UK) for helpful discussions.

DECLARATION OF INTERESTS

The authors declare no competing interests.

REFERENCES

Antonny, B. (2011). Mechanisms of Membrane Curvature Sensing. Annu. Rev. Biochem. *80*, 101–123.

Bigay, J., Casella, J.-F., Drin, G., Mesmin, B. and Antonny, B. (2005). ArfGAP1 responds to membrane curvature through the folding of a lipid packing sensor motif. EMBO J. *24*, 2244–2253.

Brady, J.P., Claridge, J.K., Smith, P.G. and Schnell, J.R. (2015). A conserved amphipathic helix is required for membrane tubule formation by Yop1p. Proc. Natl. Acad. Sci. U. S. A. *112*, E639–E648.

Breeze, E., Dzimitrowicz, N., Kriechbaumer, V., Brooks, R., Botchway, S.W., Brady, J.P., Hawes, C., Dixon, A.M., Schnell, J.R., Fricker, M.D. *et al*. (2016). A C-terminal amphipathic helix is necessary for the in vivo tubule-shaping function of a plant reticulon. Proc. Natl. Acad. Sci. U. S. A*. 113*, 10902–7.

Caldwell, T.A., Baoukina, S., Brock, A.T., Oliver, R.C., Root, K.T., Krueger, J.K., Glover, K.J., Tieleman, D.P. and Columbus, L. (2018). Low- *q* Bicelles Are Mixed Micelles. J. Phys. Chem. Lett. *9*, 4469–4473.

Casal, E., Federici, L., Zhang, W., Fernandez-Recio, J., Priego, E.-M., Miguel, R.N., DuHadaway, J.B., Prendergast, G.C., Luisi, B.F. and Laue, E.D. (2006). The crystal structure of the BAR domain from human Bin1/amphiphysin II and its implications for molecular recognition. Biochemistry *45*, 12917–28.

Chen, J., Stefano, G., Brandizzi, F. and Zheng, H. (2011). Arabidopsis RHD3 mediates the generation of the tubular ER network and is required for Golgi distribution and motility in plant cells. J. Cell Sci. *124,* 2241–2252.

Chow, M., Sklepari, M., Frigerio, L. and Dixon, A.M. (2018). Bacterial expression, purification and biophysical characterization of the smallest plant reticulon isoform, RTNLB13. Protein Expr. Purif. *152*, 31–39.

Coughlan, S.J., Hastings, C. and Winfrey, R.J. (1996). Molecular characterisation of plant endoplasmic reticulum. Identification of protein disulfide-isomerase as the major reticuloplasmin. Eur. J. Biochem. *235,* 215–24.

Crooks, G.E., Hon, G., Chandonia, J.-M. and Brenner, S.E. (2004). WebLogo: A Sequence Logo Generator. Genome Res. *14,* 1188–1190.

Dixon, A.M., Venable, R.M., Pastor, R.W. and Bull, T.E. (2002). Micelle-bound conformation of a hairpin-forming peptide: Combined NMR and molecular dynamics study. Biopolymers *65*, 284–298.

Drin, G. and Antonny, B. (2010). Amphipathic helices and membrane curvature. FEBS Lett. *584,*

1840–1847.

Ford, M.G.J., Mills, I.G., Peter, B.J., Vallis, Y., Praefcke, G.J.K., Evans, P.R. and McMahon, H.T. (2002). Curvature of clathrin-coated pits driven by epsin. Nature *419,* 361–366.

Giménez-Andrés, M., Čopič, A. and Antonny, B. (2018). The Many Faces of Amphipathic Helices. Biomolecules *8*, 45.

Griffing, L.R., Lin, C., Perico, C., White, R.R. and Sparkes, I. (2017). Plant ER geometry and dynamics: biophysical and cytoskeletal control during growth and biotic response. Protoplasma *254,* 43–56.

He, H.-T. and Bongrand, P. (2012). Membrane dynamics shape TCR-generated signaling. Front. Immunol. *3***,** 90.

Hu, J., Shibata, Y., Voss, C., Shemesh, T., Li, Z., Coughlin, M., Kozlov, M.M., Rapoport, T.A. and Prinz, W.A. (2008). Membrane proteins of the endoplasmic reticulum induce high-curvature tubules. Science *319*, 1247–1250.

Jao, C.C., Hegde, B.G., Chen, J., Haworth, I.S. and Langen, R. (2008). Structure of membrane-bound alpha-synuclein from site-directed spin labeling and computational refinement. Proc. Natl. Acad. Sci. U. S. A*. 105,* 19666–71.

Jarsch, I.K., Daste, F. and Gallop, J.L. (2016). Membrane curvature in cell biology: An integration of molecular mechanisms. J. Cell Biol. *214*, 375–387.

Jensen, M.B., Bhatia, V.K., Jao, C.C., Rasmussen, J.E., Pedersen, S.L., Jensen, K.J., Langen, R. and Stamou, D. (2011). Membrane curvature sensing by amphipathic helices: a single liposome study using α-synuclein and annexin B12. J. Biol. Chem. *286*, 42603–14.

Madeira, F., Park, Y.M., Lee, J., Buso, N., Gur, T., Madhusoodanan, N., Basutkar, P., Tivey, A.R.N., Potter, S.C., Finn, R.D. *et al*. (2019). The EMBL-EBI search and sequence analysis tools APIs in 2019. Nucleic Acids Res*. 47*, W636–W641.

Maier, O., Galan, D.L., Wodrich, H. and Wiethoff, C.M. (2010). An N-terminal domain of adenovirus protein VI fragments membranes by inducing positive membrane curvature. Virology *402*, 11–19.

Mayer, M. and Meyer, B. (1999). Characterization of Ligand Binding by Saturation Transfer Difference NMR Spectroscopy. Angew. Chemie Int. Ed. *38*, 1784–1788.

Miyashita, N. and Koga, H. (2017). Three-dimensional ultrastructure of feeding tubes and interconnected endoplasmic reticulum in root-knot nematode-induced giant cells in rose balsam. Protoplasma *254,* 1941–1951.

Morton, L.A., Yang, H., Saludes, J.P., Fiorini, Z., Beninson, L., Chapman, E.R., Fleshner, M., Xue, D., and Yin, H. (2013) MARCKS-ED peptide as a curvature and lipid sensor. ACS Chem. Biol. *8*, 218-225.

Oertle, T., Klinger, M., Stuermer, C.A.O. and Schwab, M.E. (2003). A reticular rhapsody: phylogenic evolution and nomenclature of the RTN/Nogo gene family. FASEB J. *17*, 1238–1247.

Pettersen, E.F., Goddard, T.D., Huang, C.C., Couch, G.S., Greenblatt, D.M., Meng, E.C. and Ferrin, T.E. (2004). UCSF Chimera—A visualization system for exploratory research and analysis. J. Comput. Chem. *25*, 1605–1612.

Pitcher III, W.H. and Huestis, W.H. (2002). Preparation and analysis of small unilamellar phospholipid vesicles of a uniform size. Biochem. Biophys. Res. Commun. *296*, 1352–1355.

Pranke, I.M., Morello, V., Bigay, J., Gibson, K., Verbavatz, J.-M., Antonny, B. and Jackson, C.L. (2011). α-Synuclein and ALPS motifs are membrane curvature sensors whose contrasting chemistry mediates selective vesicle binding. J. Cell Biol. *194*, 89–103.

Ramamurthi, K.S., Lecuyer, S., Stone, H.A. and Losick, R. (2009). Geometric cue for protein localization in a bacterium. Science *323*, 1354–7.

Ramamurthi, K.S. and Losick, R. (2009). Negative membrane curvature as a cue for subcellular localization of a bacterial protein. Proc. Natl. Acad. Sci. U. S. A. *106*, 13541–5.

Sato, H. and Feix, J.B. (2006). Peptide–membrane interactions and mechanisms of membrane destruction by amphipathic α-helical antimicrobial peptides. Biochim. Biophys. Acta - Biomembr. *1758*, 1245–1256.

Schweitzer, Y., Shemesh, T. and Kozlov, M.M. (2015). A Model for Shaping Membrane Sheets by Protein Scaffolds. Biophys. J*. 109*, 564–573.

Shibata, Y., Voss, C., Rist, J.M., Hu, J., Rapoport, T.A., Prinz, W.A. and Voeltz, G.K. (2008). The reticulon and DP1/Yop1p proteins form immobile oligomers in the tubular endoplasmic reticulum. J. Biol. Chem*. 283*, 18892–18904.

Snead, D., Wragg, R.T., Dittman, J.S. and Eliezer, D. (2014). Membrane curvature sensing by the C-terminal domain of complexin. Nat. Commun. *5*, 4955.

Sparkes, I., Tolley, N., Aller, I., Svozil, J., Osterrieder, A., Botchway, S., Mueller, C., Frigerio, L. and Hawes, C. (2010). Five Arabidopsis reticulon isoforms share endoplasmic reticulum location, topology, and membrane-shaping properties. Plant Cell *22*, 1333–1343.

Sreerama, N. and Woody, R.W. (2000). Estimation of protein secondary structure from circular dichroism spectra: comparison of CONTIN, SELCON, and CDSSTR methods with an expanded reference set. Anal. Biochem. *287*, 252–260.

Tieleman, D.P., van der Spoel, D., and Berendsen, H.J.C. (2000). Molecular Dynamics Simulations of Dodecylphosphocholine Micelles at Three Different Aggregate Sizes: Micellar Structure and Chain Relaxation. J. Phys. Chem. B *104*, 6380-6388.

UniProt: a worldwide hub of protein knowledge. (2019). Nucleic Acids Res. *47*, D506–D515.

van Stokkum, I.H., Spoelder, H.J., Bloemendal, M., van Grondelle, R. and Groen, F.C. (1990). Estimation of protein secondary structure and error analysis from circular dichroism spectra. Anal. Biochem. *191*, 110–118.

Vanni, S., Hirose, H., Barelli, H., Antonny, B. and Gautier, R. (2014). A sub-nanometre view of

how membrane curvature and composition modulate lipid packing and protein recruitment. Nat. Commun. *5*, 4916.

Voeltz, G.K., Prinz, W.A., Shibata, Y., Rist, J.M. and Rapoport, T.A. (2006). A class of membrane proteins shaping the tubular endoplasmic reticulum. Cell *124*, 573–586.

Vollmer, B., Schooley, A., Sachdev, R., Eisenhardt, N., Schneider, A.M., Sieverding, C., Madlung, J., Gerken, U., Macek, B. and Antonin, W. (2012). Dimerization and direct membrane interaction of Nup53 contribute to nuclear pore complex assembly. EMBO J. *31*, 4072–4084.

Vranken, W.F., Boucher, W., Stevens, T.J., Fogh, R.H., Pajon, A., Llinas, M., Ulrich, E.L., Markley, J.L., Ionides, J. and Laue, E.D. (2005). The CCPN data model for NMR spectroscopy: Development of a software pipeline. Proteins Struct. Funct. Bioinforma*. 59*, 687–696.

West, M., Zurek, N., Hoenger, A. and Voeltz, G.K. (2011). A 3D analysis of yeast ER structure reveals how ER domains are organized by membrane curvature. J. Cell Biol. *193*, 333–346.

Westrate, L.M., Lee, J.E., Prinz, W.A. and Voeltz, G.K. (2015). Form Follows Function: The Importance of Endoplasmic Reticulum Shape. Annu. Rev. Biochem. *84*, 791–811.

Whitmore, L. and Wallace, B.A. (2004). DICHROWEB, an online server for protein secondary structure analyses from circular dichroism spectroscopic data. Nucleic Acids Res. *32*, W668–W673.

Wishart, D.S., Sykes, B.D. and Richards, F.M. (1992). The chemical shift index: a fast and simple method for the assignment of protein secondary structure through NMR spectroscopy. Biochemistry *31*, 1647–1651.

Wu, D.H., Chen, A.D. and Johnson, C.S. (1995). An Improved Diffusion-Ordered Spectroscopy Experiment Incorporating Bipolar-Gradient Pulses. J. Magn. Reson. Ser. A. *115*, 260–264.

Yokota, E., Ueda, H., Hashimoto, K., Orii, H., Shimada, T., Hara-Nishimura, I. and Shimmen, T. (2011). Myosin XI-dependent formation of tubular structures from endoplasmic reticulum isolated from tobacco cultured BY-2 cells. Plant Physiol*. 156*, 129–43.

Yue, B., Huang, C.-Y., Nieh, M.-P., Glinka, C.J. and Katsaras, J. (2005). Highly Stable Phospholipid Unilamellar Vesicles from Spontaneous Vesiculation: A DLS and SANS Study. J. Phys. Chem. B. *109*, 609–616.

TABLES

Table 1. Properties of the membrane mimetics tested in this study and their impact on the helical composition of the RTNLB13 APH peptides studied here. The hydrodynamic diameter ($d_{avg} \pm$ standard deviation) of each mimetic was measured by dynamic light scattering, and correlated with the helical content of the peptide (% helix) as obtained from fitting of circular dichriosm data using Dichroweb. The detergent micelle aggregation number (N_A), length and saturation of the acyl chain, and head group charge are given.

Mimetic	**d_{avg}, nm**	**% helix**			**Chain**	**Charge**
		16-mer	18-mer	22-mer		
LMPG[a] (N_A 55)	3.9 ± 0.4	55	79	69	14	Anionic
DPC[b] (N_A 70–80)	4.1 ± 0.5	37	68	65	12	Zwitterionic
DDM[c] (N_A 98)	5.7 ± 0.9	10	48	73	12	Nonionic
DHPC[d]:DMPC[e] q=0.25	18.2 ± 4.3	21	34	46	6/14:0	Zwitterionic
DHPC:DMPC q=0.5	22.5 ± 1.8	7	7	35	6/14:0	Zwitterionic
DHPC:DMPC q=0.75	26.6 ± 2.4	8	32	26	6/14:0	Zwitterionic
9:1 DLPC[f]:DLPA[g]	39.4 ± 9.5	5	7	6	12:0	Anionic
DOPC[h]	54.6 ± 2.2	6	7	7	18:1	Zwitterionic
DLPC	57.1 ± 6.3	4	7	4	12:0	Zwitterionic
85:15 DOPC:DOPE[i]	57.6 ± 2.8	5	5	5	18:1	Zwitterionic
Soy polar lipids	58.3 ± 0.1	3	-	15	mixed	Anionic
DMPC	59.1 ± 0.1	6	7	6	14:0	Zwitterionic
POPC[j]	70.2 ± 1.5	6	10	8	16:0-18:1	Zwitterionic
DEPC[k]	82.7 ± 24	5	9	11	22:1	Zwitterionic

Footnotes: [a]LMPG, 1-myristoyl-2-hydroxy-sn-glycero-3-phospho-(1'-rac-glycerol); [b]DPC, n-dodecylphosphocholine; [c]DDM, n-dodecyl-ß-D-maltoside; [d]DHPC, 1,2-dihexanoyl-sn-glycero-3-phosphocholine; [e]DMPC, 1,2-dimyristoyl-sn-glycero-3-phosphocholine; [f]DLPC, 1,2-dilauroyl-sn-glycero-3-phosphocholine; [g]DLPA, 1,2-dilauroyl-sn-glycero-3-phosphate; [h]DOPC, 1,2-dioleoyl-sn-glycero-3-phosphocholine; [i]DOPE, 1,2-dioleoyl-sn-glycero-3-phosphoethanolamine; [j]POPC, 1-palmitoyl-2-oleoyl-glycero-3-phosphocholine; [k]DEPC, 1,2-dierucoyl-sn-glycero-3-phosphocholine

Table 2. Experimental Diffusion Coefficients (D.C.) for R13-APH$_{22,}$ DPC (mimetic) and DMPC (mimetic), and the peptide-mimetic solutions.

The last column states the fraction of peptide bound to the mimetics, as indicated by the diffusion data. All measurements were made in 100% D_2O buffer at 310 K.

	R13-APH$_{22}$ D.C. ($\times 10^{10}$ m^2/s)	Mimetic D.C. ($\times 10^{10}$ m^2/s)	f_{bound}
Buffer	2.12 ± 0.03		
DPC	1.23 ± 0.12	1.28 ± 0.003	1.06
DMPC	2.09 ± 0.13	0.17 ± 0.003	0.02

FIGURE CAPTIONS

Figure 1. Front views of the amphipathic helical regions of (A) worm complexin, (B) ArfGAP1 amphipathic lipid packing sensor (ALPS) motif, and (C) α-Synuclein, and the various mechanisms by which these APHs can bind to lipid membranes by membrane curvature recognition. **(A)** The less well-defined amphipathic helix in complexin initially binds to a curved membrane in a disordered state and undergoes a transition to a helix only after inserting its hydrophobic residues into lipid-packing defects that are a direct consequence of introducing curvature to a membrane. **(B)** Similarly, ALPS motifs can only bind to curved membranes by insertion of bulky hydrophobic amino-acids (yellow) between the acyl-chains of lipids. **(C)** α-synuclein depends on both a high degree of curvature and the presence of negatively charged lipids in order to bind to a membrane, due to its small number of hydrophobic residues (yellow) and its zwitterionic polar face. Color code: yellow, hydrophobic; purple, polar; red, anionic; blue, cationic.

Figure 2. (A) Proposed topology for the reticulon homology domain, including four transmembrane domains (1-4) and a C-terminal amphipathic helix (APH). **(B)** Wedging of transmembrane domains is thought to generate membrane curvature. **(C)** Sequence of RTNLB13 in region thought to contain the APH, immediately C-terminal to transmembrane domain 4. The three peptides studied in this work are shown below the sequence, along with their hydrophobic moments (μ) and isoelectric points (pI). Also shown in the sequence is the location of an Ile residue in the APH (shown in bold) which, when mutated to Lys, reduced tubule formation.

Figure 3. (A) CD spectra of R13-APH_{16} peptide (70 μM) in phosphate buffer and a range of detergent micelles (5–300 mM) of varying aggregation number and surface charge as summarized in Table 1. The peptide displays random coil secondary structure in buffer and DDM micelles, and helical structure in DPC and LMPG. Inset, increasing concentrations of LMPG lead to a dose-dependent increase in negative ellipticity at 222 nm. **(B)** CD spectra of R13-APH_{16}

peptide (70 μM) in DMPC lipid vesicles and DHPC:DMPC mixed micelles (bicelles) prepared with various *q* values. The peptide displays random coil secondary structure in all but *q* = 0.25 bicelles, where a small degree of helicity can be observed. All CD data are given in units of mean residue ellipticity (MRE, deg cm^2 $dmol^{-1}$). **(C)** Plot of percent helical content of the R13-APH_{16} peptide (obtained from fitting of circular dichroism data using Dichroweb software) versus the hydrodynamic diameter of the membrane mimetic used (obtained from dynamic light scattering measurements). Inset shows analogous data for residues 2-23 of human α-synuclein and the ALPS motif in rat ArfGAP1, residues 199-223.

Figure 4. Survey of NMR-derived sequential backbone NOE connectivities for the R13-APH_{16} peptide solubilized in DPC-d_{38}, classified as strong, weak, or absent by the thickness (or absence) of a bar connecting the residues involved. The non-sequential connectivities listed (*i.e*. i, i + n) are unique to helices, and were used alongside chemical shift index analyses (CSI) to localize the amphipathic helix to residues Glu_{160}–Leu_{169} (underlined in sequence).

Figure 5. (A) Helical wheel plots of R13-APH_{18} (left) and R13-APH_{22} (right) peptides. **(B)** Plot of percent helical content of the R13-APH_{18} (●) and R13-APH_{22} (○) peptides (obtained from fitting of circular dichroism data using Dichroweb) versus the hydrodynamic diameter of the membrane mimetic used (obtained from DLS measurements). Inset, tryptophan fluorescence emission spectra of R13-APH_{18} and R13-APH_{22} in buffer, and with DPC and DMPC. **(C)** Survey of NMR-derived sequential backbone NOE connectivities for the R13-APH_{22} peptide solubilized in DPC-d_{38}, classified as strong, weak, or absent by the thickness (or absence) of a bar connecting the residues involved. The non-sequential connectivities listed (*i.e.* i, i + n) are unique to helices, and were used alongside chemical shift index analyses (CSI) to localize the amphipathic helix to residues Lys_{156}–Leu_{169} (underlined in sequence). **(D)** Sequence logo indicating the degree of

conservation of the 22-residue peptide amongst all reticulon-like protein isoforms in *A. Thaliana*, with the exception of RTNLB19 and RTNLB20.

Figure 6. CD spectra of R13-APH22 peptide in the presence of vesicles with identical lipid composition but increasing diameter. The lipid composition was maintained at 60:1:15 DMPC:DMPG:DHPC and the size was modulated between 23-116 nm. Inset shows plot of mean residue ellipticity at 222 nm and percentage helicity as obtained from fitting of the data in Dichroweb versus vesicle diameter.

Figure 7. (A) 1D ^{1}H NMR spectrum of R13-APH$_{22}$ with 50 mM DPC in 90% H_2O/10% D_2O buffer. **(B)** 1D ^{1}H NMR spectrum of R13-APH$_{22}$ with 50 mM DPC in 100% D_2O buffer. Backbone amide protons that are less solvent accessible are labelled. **(C)** 1D ^{1}H STD-NMR spectrum of R13-APH$_{22}$ with 50 mM DPC in 100% D_2O buffer. The non-exchangeable protons that have undergone saturation transfer are labelled. **(D)** Helical wheel representation of the RTNLB13 APH, as identified from NMR structural studies, with those protons on the hydrophobic face that have been identified as important for binding/helix formation indicated via the method used to elucidate this information. **(E)** Helical wheel representations comparing the hydrophobic penetration depth of known curvature-responsive helices in ArfGAP1 (known as amphipathic lipid packing sensors, or ALPS), α-synuclein, and RTNLB13 with that of known antimicrobial peptides Aurein, Magainin 1 and Mastoparan.

FIGURES

Figure 1.

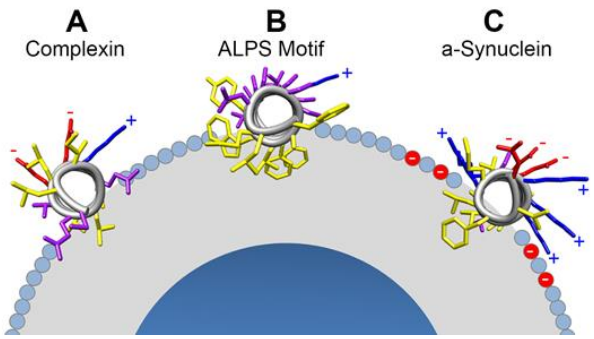

Figure 2.

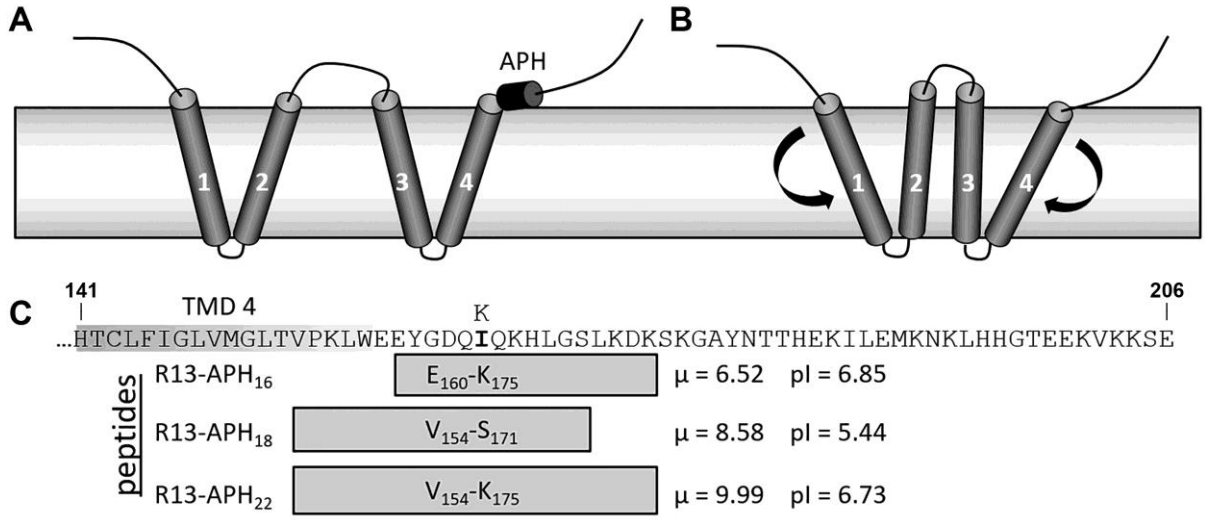
A
APH
1
2
3
4
B
1
2
3
4
C
141
TMD 4
K
206
…HTCLFIGLVMGLTVPKLWEEYGDQIQKHLGSLKDKSKGAYNTTHEKILEMKNKLHHGTEEKVKKSE
peptides
R13-APH16
E160-K175
μ = 6.52 pI = 6.85
R13-APH18
V154-S171
μ = 8.58 pI = 5.44
R13-APH22
V154-K175
μ = 9.99 pI = 6.73

Figure 3.

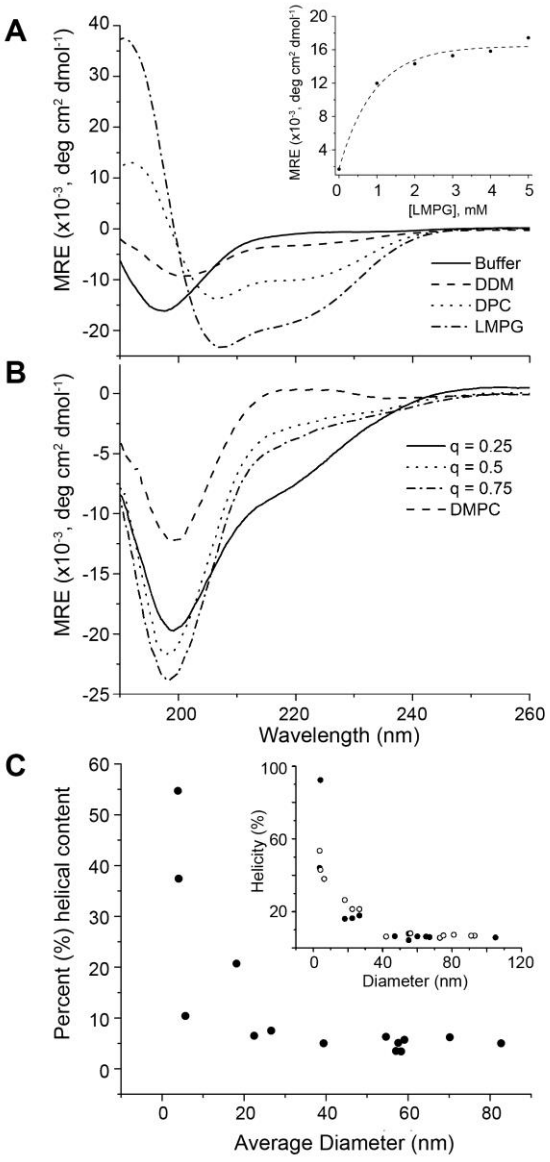
A
MRE (x10-3, deg cm2 dmol-1)
Buffer
DDM
DPC
LMPG
[LMPG], mM
B
MRE (x10-3, deg cm2 dmol-1)
q = 0.25
q = 0.5
q = 0.75
DMPC
Wavelength (nm)
C
Percent (%) helical content
Helicity (%)
Diameter (nm)
Average Diameter (nm)

Figure 4.

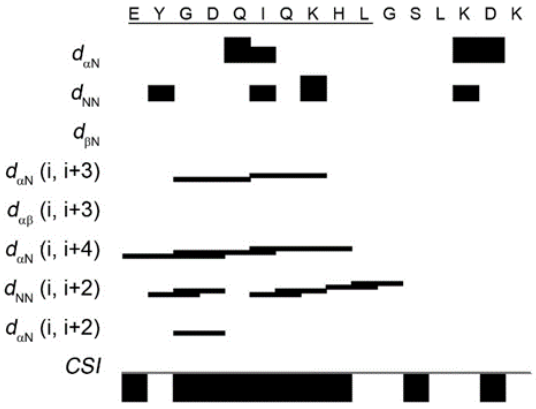
E Y G D Q I Q K H L G S L K D K
$d_{\alpha N}$
d_{NN}
$d_{\beta N}$
$d_{\alpha N}$ (i, i+3)
$d_{\alpha\beta}$ (i, i+3)
$d_{\alpha N}$ (i, i+4)
d_{NN} (i, i+2)
$d_{\alpha N}$ (i, i+2)
CSI

Figure 5.

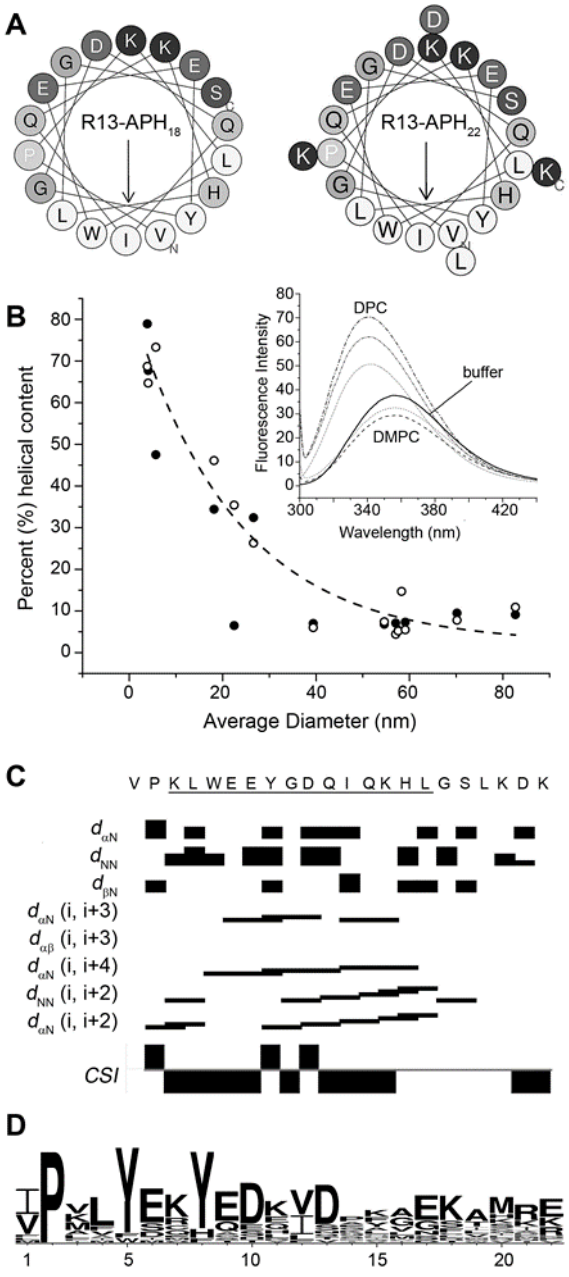
A
R13-APH18
R13-APH22
B
Percent (%) helical content
Average Diameter (nm)
Fluorescence Intensity
Wavelength (nm)
DPC
buffer
DMPC
C
V P K L W E E Y G D Q I Q K H L G S L K D K
dαN
dNN
dβN
dαN (i, i+3)
dαβ (i, i+3)
dαN (i, i+4)
dNN (i, i+2)
dαN (i, i+2)
CSI
D

Figure 6.

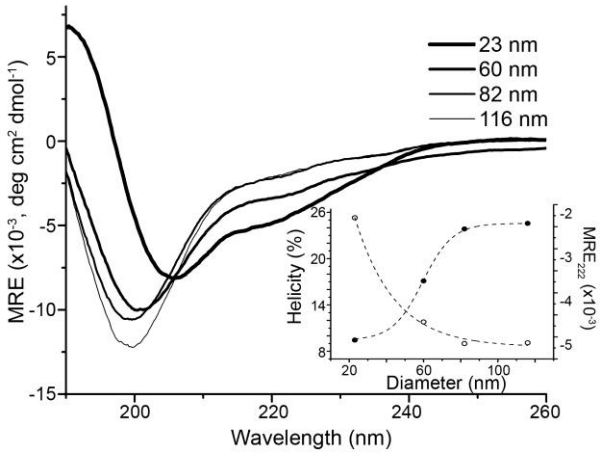
23 nm
60 nm
82 nm
116 nm
MRE (x10-3, deg cm2 dmol-1)
Wavelength (nm)
Helicity (%)
MRE222 (x10-3)
Diameter (nm)

Figure 7.

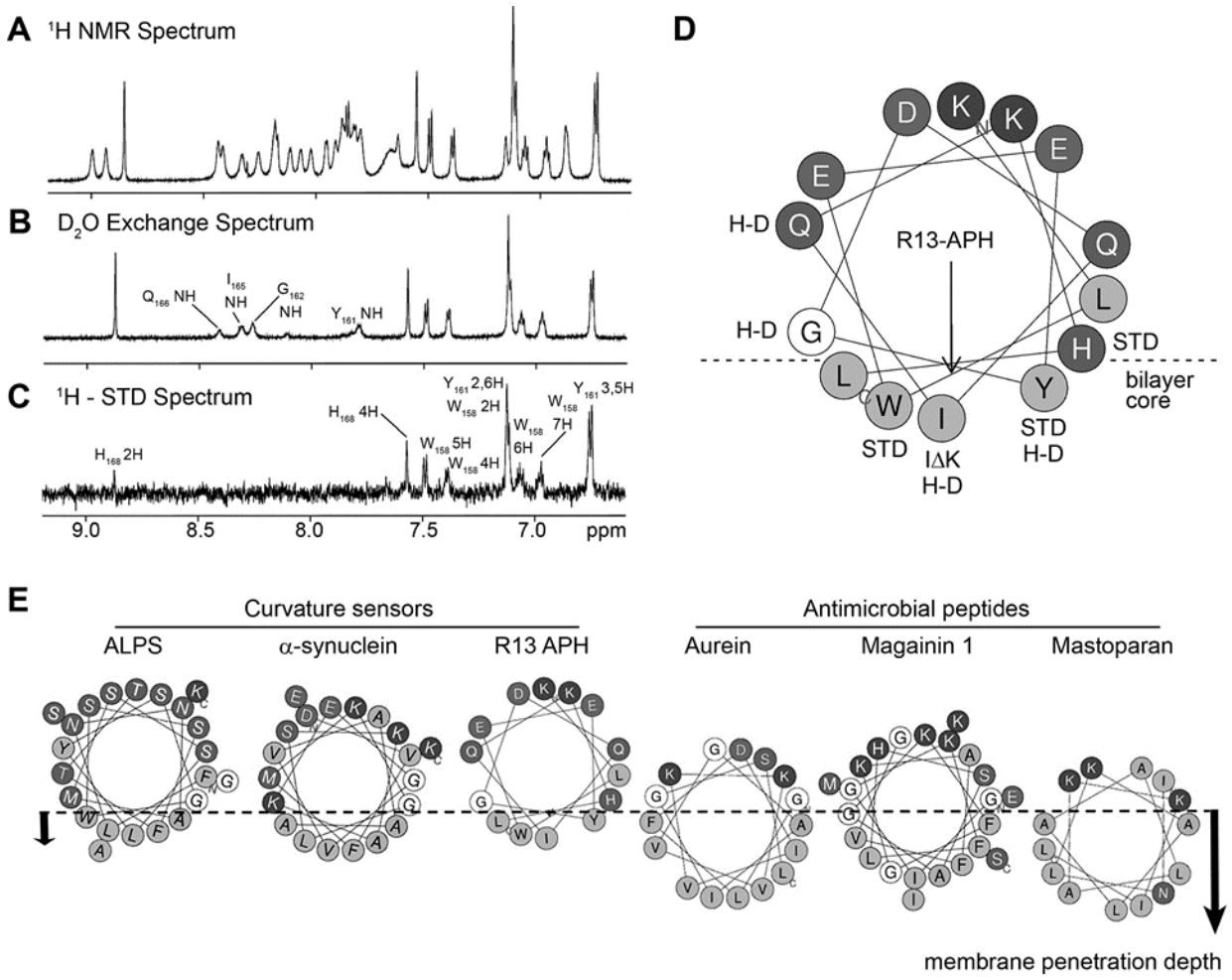
A ¹H NMR Spectrum
B D₂O Exchange Spectrum
Q166 NH
I165 NH
G162 NH
Y161 NH
C ¹H - STD Spectrum
H168 2H
H168 4H
W158 5H
W158 4H
Y161 2,6H
W158 2H
W158 7H
6H
Y161 3,5H
9.0
8.5
8.0
7.5
7.0
ppm
D
R13-APH
H-D
H-D
STD
bilayer core
STD
IΔK H-D
STD H-D
E
Curvature sensors
ALPS
α-synuclein
R13 APH
Antimicrobial peptides
Aurein
Magainin 1
Mastoparan
membrane penetration depth